

HIGH-ORDER DISCONTINUOUS GALERKIN METHODS: SIMULATION OF COIL FLOWS

I. PIVKIN, R.M. KIRBY AND G.E. KARNIADAKIS
Division of Applied Mathematics
Brown University

Abstract.

We have developed spectral methods in the discontinuous Galerkin framework appropriate for simulations of high-speed flows in complex-geometry domains. In this paper we present details of the stability of the method and demonstrate the importance of over-integration for strongly nonlinear problems. We then present results from the application of the method to stability studies of supersonic and subsonic flows in a Chemical Oxygen Iodine Laser (COIL) device.

1. Introduction

Finite volume methods have been very successful in simulating steady high-speed flows but they are rather inefficient for unsteady flow simulations, and especially for direct or large eddy simulations of turbulent and transitional compressible flows. Discontinuous Galerkin Methods (DGM) [1], when combined with high-order discretizations as in [2], offer some of the advantages of finite volume methods and lead to numerical solutions with significantly reduced numerical dispersion and dissipation. In summary, high-order DGM are:

- High-order finite volumes applied to structured or unstructured meshes.
- Flux-based, and thus maintain conservativity which is important for correct shock location and long-time integration.
- L_2 -stable, and thus they do not require explicit flux limiters.
- Robust as they employ Riemann solvers.

The particular DGM implementation we have developed employs an *orthogonal* polynomial basis of different order in each element. The discon-

tinuous basis is orthogonal, hierarchical, and maintains a tensor-product property even for non-separable domains [3, 4].

Unlike pseudo-spectral (collocation) methods used often for incompressible flow simulations, in our spectral DGM approach the number of quadrature points and the number of degrees of freedom (i.e., modes) are decoupled in each element. Specifically, it is a super-collocation method combined with Galerkin projections in an element-wise fashion. This is very important for the treatment of nonlinear terms as this approach offers the possibility of *dealiasing* on arbitrarily non-uniform grids. We discuss this issue in detail in the next section, where we show that simple *quadrature-modes rules* can be derived by considering the long-term (asymptotic) stability of DGM.

In the last section, we apply DGM to three-dimensional supersonic and subsonic flows in a Chemical Oxygen Iodine Laser (COIL) configuration. The flow field of a COIL typically contains multi-phase flow (oxygen, iodine and helium) as well as chemical reactions [5], but here we consider the stability of cold (helium) flow. Due to the importance of COILs in military and industrial uses, there has been a lot of research focused on them during the last decade [6, 7, 8]. Recent two-dimensional simulations have shown that the supersonic COIL flow is unsteady although corresponding preliminary simulations have shown substantially reduced temporal variations [9]. In the current work, we consider both supersonic as well as subsonic conditions on different grids and with p-refinement to address more systematically the question of unsteadiness. Our results show that the strong compressibility and the symmetric crossflow stabilize the supersonic nozzle flow, in contrast with the subsonic cases.

2. Discontinuous Galerkin Method - DGM

We consider the non-dimensional compressible Navier-Stokes equations, which we write in compact form as

$$\vec{U}_t + \nabla \cdot \mathbf{F} = Re_\infty^{-1} \nabla \cdot \mathbf{F}^\nu \quad \text{in } \Omega \quad (1)$$

where \mathbf{F} and \mathbf{F}^ν correspond to inviscid and viscous flux contributions, respectively, and Re_∞ is the reference Reynolds number. Here the vector $\vec{U} = [\rho, \rho u_1, \rho u_2, \rho u_3, \rho e]^t$ with $\mathbf{u} = (u_1, u_2, u_3)$ the local fluid velocity, ρ the fluid density, and e the total energy. Splitting the Navier-Stokes operator in this form allows for a separate treatment of the inviscid and viscous contributions, which, in general, exhibit different mathematical properties.

To give an overview of the formulation we first apply DGM to the linear two-dimensional equation for advection of a conserved quantity u

$$\frac{\partial u}{\partial t} + \nabla \cdot \mathbf{F}(u) = 0, \quad (2)$$

where $\mathbf{F}(u) = (f(u), g(u), h(u))$ is the *flux* vector which defines the transport of $u(\mathbf{x}, t)$. We start with the variational statement of the standard Galerkin formulation of (2) by multiplying by a test function v and integrating by parts

$$\int_{\Omega} \frac{\partial u}{\partial t} v \, dx + \int_{\partial\Omega} v \hat{\mathbf{n}} \cdot \mathbf{F}(u) \, ds - \int_{\Omega} \nabla v \cdot \mathbf{F}(u) \, dx = 0. \quad (3)$$

The solution $u \in \mathcal{X}$ (approximation space) satisfies this equation for all $v \in \mathcal{V}$ (test space), where \mathcal{X} may contain discontinuous functions. The discrete space \mathcal{X}^{δ} contains polynomials within each “element,” but zero outside the element. Here the “element” is, for example, an individual triangular region T_i in the computational mesh applied to the problem. Thus, the computational domain $\Omega = \bigcup_i T_i$, and T_i, T_j overlap only on edges.

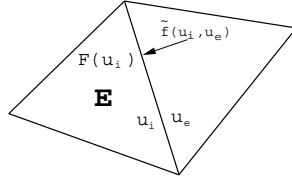


Figure 1. Interface conditions between two adjacent triangles.

Each element (E) is treated separately, giving a variational statement (after integrating by parts once more):

$$\frac{\partial}{\partial t} (u, v)_E + \int_{\partial T_E} v (\tilde{f}(u_i, u_e) - \mathbf{F}(u_i)) \cdot \mathbf{n} \, ds + (\nabla \cdot \mathbf{F}(u), v)_E = 0, \quad (4)$$

where $\mathbf{F}(u_i)$ is the flux of the interior values. Computations on each element are performed separately, and the connection between elements is a result of the way boundary conditions are applied. Here, boundary conditions are enforced via the numerical surface flux $\tilde{f}(u_i, u_e)$ that appears in equation (4). Because this value is computed at the boundary between adjacent elements, it may be computed from the value of u given at either element. These two possible values are denoted here as u_i in the interior of the element under consideration and u_e in the exterior (see figure 1). Upwinding considerations dictate how this flux is computed.

In the more complicated case of a hyperbolic system of equations, an approximate Riemann solver should be used to compute a value of f, g, h (in three-dimensions) based on u_i and u_e . Specifically, we compute the flux $\tilde{f}(u_i, u_e)$ using upwinding, i.e.

$$\tilde{f}(u) = R\Lambda^+ L u_i + R\Lambda^- L u_e$$

where A (the Jacobian matrix of F) is written in terms of the left and right eigenvectors, i.e. $A = R\Lambda L$ with Λ containing the corresponding eigenvalues in the diagonal; also, $\Lambda^\pm = (\Lambda \pm |\Lambda|)/2$. Alternatively, we can use a standard Lax-Friedrichs flux

$$\tilde{f}(u) = \frac{1}{2}(f(u_e) + f(u_i)) - \frac{1}{2}R|\Lambda|L(u_e - u_i).$$

In order to solve the compressible Navier-Stokes equations we also need to treat the second-order terms. This is done similarly by introducing auxiliary fluxes and constructing a system of first-order equations that we treat similarly as the advection equation above. The difference is in the choice of the numerical fluxes at the interface, which we have taken here to be the arithmetic mean of the fluxes from adjoint elements. However, other choices are possible that can affect the computational complexity and the accuracy [1].

With regard to the trial basis we employ Jacobi polynomials with variable weights as reported in [2]. The degree of polynomial can be varied from one element to the other but interpolation along edges or elemental faces should involve the higher order polynomial in order to maintain conservativity. The DGM method is L_2 -stable but in practice instabilities may arise in under-resolved or marginally resolved simulations. Such instabilities were first reported in [2] where a slight over-integration seem to provide long-time integration stability. In the next section, we revisit this issue and provide more details on over-integration for both quadratic as well as cubic nonlinearities.

2.1. STABILITY AND OVER-INTEGRATION

To understand the ramifications of under-integration of nonlinear terms, we performed the following test:

1. Initialize a single element spanning $[-1, 1]$ and containing 16 modes.
2. Initialize all the modal coefficients to one.
3. Evaluate the modal representation on a set of quadrature points q .
4. Pointwise square the values at the quadrature points.
5. Pre-multiply the set of points (as a vector) by the collocation derivative matrix of the appropriate size (rank $q \times q$).
6. Project back to modal coefficients by discrete inner products using Gaussian integration.

The procedure above mimicks the “physical space” or pseudo-spectral evaluation of the term $\frac{\partial u^2}{\partial x}$ commonly used in spectral methods for evaluating nonlinear terms. This test was chosen because even in its simplicity it

models the order of nonlinearity that occurs in the solution of the incompressible Navier-Stokes equations. All modes are set to one to mimick a case in which an element has under-resolved or marginally resolved the solution within the element. In the test above, the only unspecified parameter is the number of quadrature points q to be used. In using Gauss-Lobatto points, the value of q is taken to be one more than the number of modes M (in this case then $M = 16$ and $q = 17$) [2], but this value is appropriate for the inner products corresponding to linear terms. For a quadratic or cubic nonlinearities more quadrature points are required. The ramifications of under-integration of this form are shown in figure 2. The figure on the left was obtained for quadratic nonlinearity ($\frac{\partial}{\partial x} u^2$) and the figure on the right was obtained for a cubic nonlinearity ($\frac{\partial}{\partial x} u^3$). The difference in the modal coefficients at the conclusion of the algorithm above for different values of q is provided. We observe that for the quadratic nonlinearity, once $\frac{3}{2}M$ quadrature points are used, the difference in the modal values do not change. Similarly for the cubic nonlinearity, once $2M$ quadrature points are used, the difference in the modal values do not change.

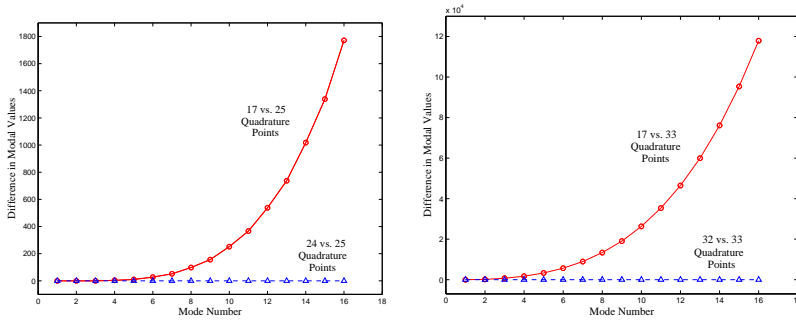


Figure 2. Comparison of the difference in modal coefficients when different numbers of quadrature points are used. Quadratic nonlinearity on the left and cubic nonlinearity on the right.

If figure 3 we plot the difference between using the $\frac{3}{2}M$ rule and $2M$ rule (left and right figures, respectively) versus $M + 2$ rule for choosing the number of quadrature points q . Observe that for small number of modes the two regions overlap or may be sufficiently close that using $M + 2$ will not lead to aliasing instabilities. This may be an explanation of the results shown in [2] in which over-integration by one point was sufficient to stabilize the flow simulation.

To further test the integration of the nonlinear terms, we chose to solve viscous Burgers equation with $\nu = 10^{-5}$. Five equally spaced elements spanning $[-1, 1]$ were used, each one having 16 modes. We have found

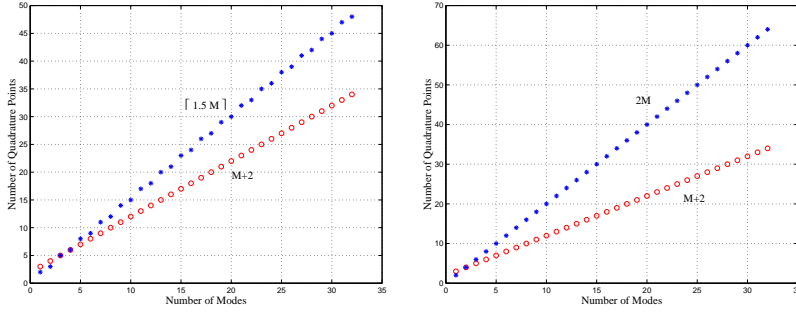


Figure 3. Difference between using the $\frac{3}{2}M$ rule and $2M$ rule (left and right figures, respectively) versus $(M + 2)$ rule for choosing the number of quadrature points q .

that when using 17, 19 and 21 quadrature points, the solution is unstable (measured by the L_2 norm). Once the number of quadrature points reaches 24 ($\frac{3}{2}M$, where M is the number of modes), the L_2 norm of the solution does not change.

3. Simulation of COIL Flows

The chemical oxygen iodine laser (COIL) is a very powerful laser, capable of producing megawatts of continuous power at short wavelengths (1315 nm). There are two distinct types of COIL configurations, depending on the characteristic flow velocity of the constituent gases. In the first one, the *supersonic lasers*, the velocities are of the order of 400 m/s or higher while in the second type, the *subsonic lasers*, the characteristic velocities are an order of magnitude lower. There has been some uncertainty regarding the stability of the COIL flows, especially in the supersonic regime. Two-dimensional computations show that the flow is unstable to small perturbations and becomes oscillatory with frequency of about 40 KHz [9]. On the other hand, preliminary three-dimensional simulations reported recently in [9] show only extremely small time variations in amplitude. Unfortunately, there are not enough experimental measurements or flow visualizations to document the stability of the COIL flows, especially in the supersonic nozzle (the so-called RADICL nozzle). In this work, we study the stability of COIL flows via direct numerical simulations based on the DGM spectral/ hp element method and the code NEKTAR described in the previous section; see also [1, 4].

An overview of the supersonic flow in the central part of the nozzle is shown in figure 4. There is a strong interaction between the incoming almost uniform flow and the crossflow emanating from the six nozzles. The

SUPERSONIC (CASE A)

Inflow		Pipes		Outflow	
Density	0.013066498	Density	0.039323356	Density	0.001355714
U-velo	153.3355557	U-velo	442.6130539	U-velo	1208.084843
V-velo	0	V-velo	0	V-velo	0
W-velo	0	W-velo	0	W-velo	0
Energy	12209.51111	Energy	53746.82174	Energy	1158.745548
Mach	0.152511337	Mach	0.38	Mach	3.264908

SUBSONIC (NO PIPES) (CASE B)

Inflow		Pipes		Outflow	
Density	0.013066498	Density	0	Density	0.0130896
U-velo	153.3355557	U-velo	0	U-velo	121.480094
V-velo	0	V-velo	0	V-velo	0
W-velo	0	W-velo	0	W-velo	0
Energy	29697.27213	Energy	0	Energy	29727.77876
Mach	0.097424	Mach	0	Mach	0.077138

SUBSONIC (PIPES) (CASE C)

Inflow		Pipes		Outflow	
Density	0.013066498	Density	0.039323356	Density	0.013445426
U-velo	153.3355557	U-velo	0	U-velo	121.480094
V-velo	0	W-velo	50.95079845	V-velo	0
W-velo	0	W-velo	0	W-velo	0
Energy	29697.27213	Energy	119387.5174	Energy	30553.32435
Mach	0.097424	Mach	0.2427434	Mach	0.077138

INCOMPRESSIBLE (CASE D)

Inflow		Pipes		Outflow	
U-velo	2.003558732	U-velo	0	U-velo	0
V-velo	0	V-velo	17.40503091	V-velo	0
W-velo	0	W-velo	0	W-velo	0

geometry and dimensions of the entire device are shown in figure 5. This three-dimensional “slice” is repeated twenty times (in the direction perpendicular to the page) in order to make the entire device, so there are 20 large diameter nozzles and 40 small diameter nozzles in the COIL device. We simulate only one slice, as shown in the figure, and apply periodic boundary conditions along the third direction. A typical mesh employed in the supersonic case is shown in figure 6. It consists of 10,224 hexahedra

elements with 8 layers in the z - (periodic) direction of variable order as shown in the figure. The subsonic cases were simulated with similar meshes but with 7,312 hexahedra of constant polynomial order $p = 3$. The incompressible case was simulated on a mesh consisted of 3,066 tetrahedra with polynomial order $p = 6$.

The specific flow conditions we consider are described in table 3 (all units in metric system). We have simulated in detail the following four cases: (A) Supersonic flow corresponding to experimental case described as “9257cf11” in experiments with helium; (B) Subsonic flow without transverse (secondary) flow; (C) Subsonic flow; and (D) Incompressible flow. In all cases, the geometry remains identical and so is the primary incoming flow. Only the energy input and mass flowrate from the side pipes varies in cases (2) and (3), corresponding to zero and approximately one-eighth of the primary flow, respectively. In cases (A) and (D) the secondary flow is approximately one-fourth of the primary flow.

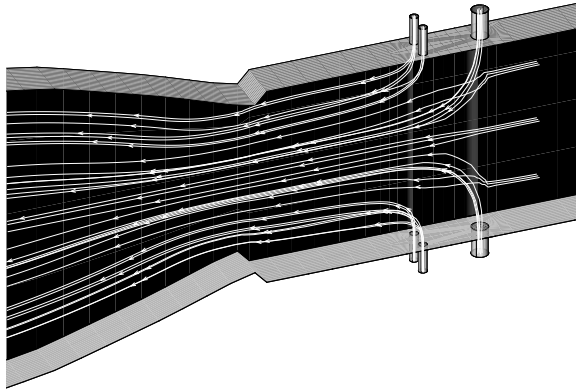


Figure 4. Streamlines in the central portion of the RADICL supersonic nozzle.

Based on systematic direct numerical simulations, we have concluded that unsteadiness is *suppressed* in the supersonic conditions similar to the ones employed in the experiments. A typical plot of Mach contours is shown in figure 7. Pressure distribution along the wall of the COIL as well as along the centerline of the COIL are shown in figure 8. Clearly, there is very good agreement of the high-order DGM results with available experimental data for the wall pressure in contrast with corresponding finite volume simulations performed here on the same mesh of figure 6 but with $p = 1$. These results were obtained from converged (in-time) simulations of the supersonic nozzle. To further examine the stability of the supersonic flow we in-

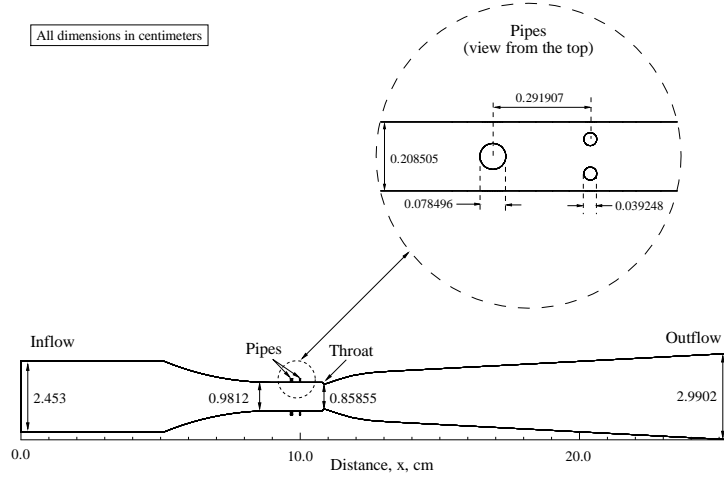


Figure 5. Geometry and dimensions of the COIL device.

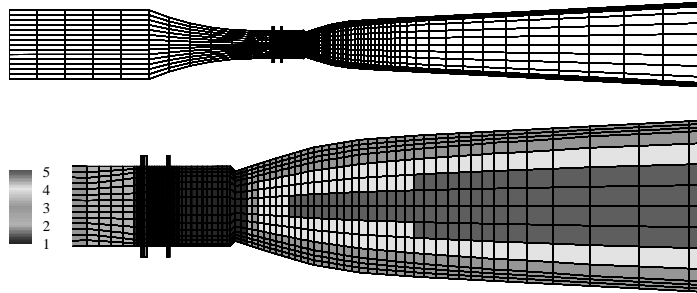


Figure 6. Mesh showing the macro-elements and corresponding polynomial order in the central part of the COIL (supersonic case).

produced an abrupt and rather large perturbation into the flow in the form of forces in all three directions corresponding to $-8,322 m/s^2$, $8,322 m/s^2$ and $8,322 m/s^2$ along the x-(streamwise), y-(crossflow) and z-(periodic)

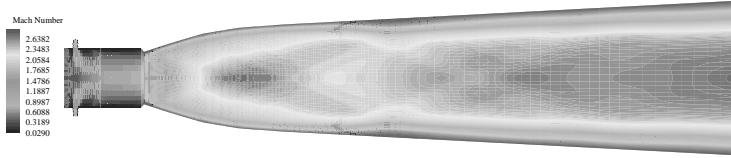


Figure 7. Mach contours in the supersonic RADICL nozzle.

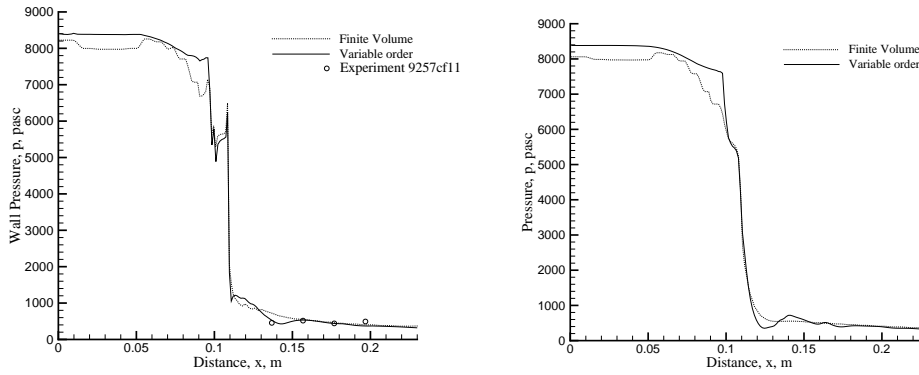


Figure 8. Pressure distribution along the wall and along the centerline for the supersonic case.

directions, respectively. This forcing was imposed for $2.39 \times 10^{-4} \text{ ms}$ and subsequently it was removed while the simulation continued. A typical result of the response in the y-momentum is shown in figure 9. We see that indeed the flow returns to steady state within a short time interval.

Unlike the supersonic case, both subsonic cases we simulated converged to time-dependent flows while the incompressible flow transitioned to a turbulent state. A typical result is shown in figure 10 that plots Mach contours of the subsonic case with crossflow; a large scale unsteadiness is present. This is shown more clearly in figure 11 where we plot the time-histories of the y-momentum of both subsonic cases. The case without crossflow shows a stationary time-periodic flow whereas the subsonic flow with crossflow exhibits an additional modulation associated with the large scale unsteadiness. Therefore, it seems that the effect of crossflow is to suppress unsteadiness.

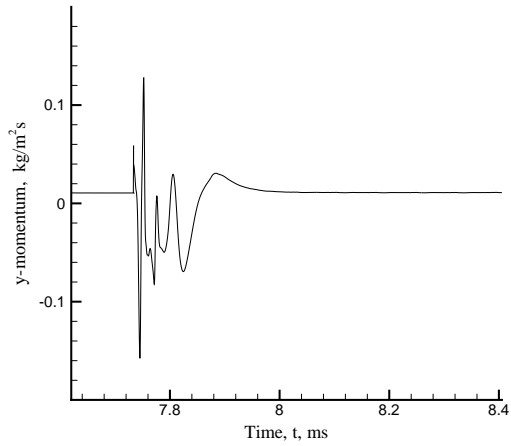


Figure 9. Time history of y -momentum for the supersonic nozzle.

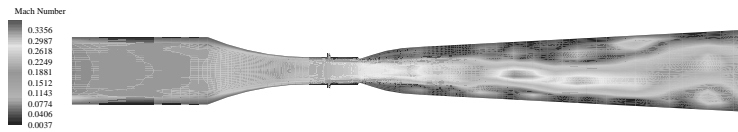


Figure 10. Mach contours for the subsonic case with crossflow.

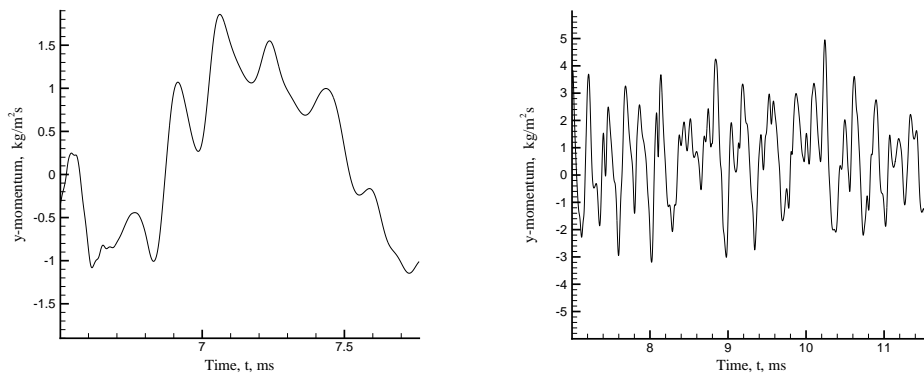


Figure 11. Time-history of y -momentum for the two subsonic cases, with crossflow (left), and without crossflow (right).

Finally, we conclude by commenting on the computational cost of the simulations. All simulations were run using an MPI-based parallel version of the method presented here with the partitioning based on a multi-level graph approach provided by the METIS software [10]. Specifically, the supersonic simulation was run on the IBM Power 3 with 0.6 seconds per time step on 80 processors, the subsonic simulations were run on the IBM Power 3 with 0.2 seconds per time step on 80 processors, and the incompressible simulation was run on the IBM SP 604e (silver nodes) with 10.7 seconds per time step on 64 processors.

Acknowledgments

This work was supported by AFOSR and computations were done on the TCASV Brown IBM SP3 and NPACI, and on the SGI O 2000 at NCSA. We would like to thank R. Canfield, T. Madden, J. Shang and J. Miller for useful discussions related to COILs.

References

1. B. Cockburn, G.E. Karniadakis, and C.-W. Shu. *Discontinuous Galerkin Methods: Theory, Computation and Applications*. Springer, 2000.
2. I. Lomtev, R.M. Kirby, and G.E. Karniadakis. A discontinuous Galerkin ALE method for viscous compressible flows in moving domains. *J. Comp. Phys.*, 155:128–159, 1999.
3. M. Dubiner. Spectral methods on triangles and other domains. *J. Sci. Comp.*, 6:345, 1991.
4. G.E. Karniadakis and S.J. Sherwin. *Spectral/hp Element Methods for CFD*. Oxford University Press, 1999.
5. J.H. Miller, J.S. Shang, R.F. Tomaro, and W.Z. Strang. Computation of COIL nozzle flowfields with transonic injection. In *AIAA-2000-2575*, 2000.
6. G.D. Hager, L.J. Watkins, R.K. Meyer, D.E. Johnson, L.J. Bean, and D.L. Loverro. A supersonic Chemical Oxygen-Iodine Laser. Technical report, Air Force Weapons Lab Technical Report 87-45, Kirtland AFB, NM, 1988.
7. M. Hishida, N. Azami, K. Iwamoto, W. Masuda, F.T. Atsuta, and M. Muro. Flow and optical fields in a supersonic flow Chemical Oxygen-Iodine Laser. In *AIAA 97-2391*, June 1997.
8. B.D. Barmashenko, D. Furman, E. Bruins, and S. Rosenwake. Iodine dissociation and small signal gain in supersonic COILS. In *AIAA 99-3427*, June 1999.
9. J.H. Miller, J.S. Shang, and T.J. Madden. Parallel computation of Chemical Oxygen/Iodine Laser flowfield. In *AIAA 2001-2869, 32nd Plasmadynamics and Lasers Conference, Anaheim, CA*, June 2001.
10. G. Karypis and V. Kumar. METIS: Unstructured graph partitioning and sparse matrix ordering system version 2.0. Technical report, Department of Computer Science, University of Minnesota, Minneapolis, MN 55455, 1995.